Cooling System Design and Thermal Analysis of Modular Stator Hybrid Excitation Synchronous Motor

Shengnan Wu, *Member, IEEE*, Daquan Hao, and Wenming Tong, *Member, IEEE*

***Abstract*—Hybrid excitation synchronous motor has the advantages of uniform and adjustable electromagnetic field, wide speed range and high power density. It has broad application prospects in new energy electric vehicles, wind power generation and other fields. This paper introduces the basic structure of hybrid excitation motor with modular stator, and analyzes the operation principle of hybrid excitation motor. The cooling structure of the water-cooled plate is designed, and the effects of the thickness of the water-cooled plate and the number of water channels in the water-cooled plate on the heat dissipation capacity of the water-cooled plate are analyzed by theoretical and computational fluid dynamics methods. The effects of different water cooling plate structures on water velocity, pressure drop, water pump power consumption and heat dissipation capacity were compared and analyzed. The influence of different inlet flow velocity on the maximum temperature rise of each part of the motor is analyzed, and the temperature of each part of the motor under the optimal water flow is analyzed. The influence of the traditional spiral water jacket cooling structure and the water-cooled plate cooling structure on the maximum temperature rise of the motor components is compared and analyzed. The results show that the water-cooled plate cooling structure is more suitable for the modular stator motor studied in this paper. Based on the water-cooled plate cooling structure, the air-water composite cooling structure is designed, and the effects of the air-water composite cooling structure and the water-cooled plate cooling structure on the maximum temperature rise of each component of the motor are compared and analyzed. The results show that the maximum temperature rise of each component of the motor is reduced under the air-water composite cooling structure.**

***Index Terms*—Hybrid excitation synchronous motor, Cooling structure of the water-cooled plate, The heat dissipation capacity of the water-cooled plate, The maximum temperature rise of each part, Air water composite cooling structure.**

Manuscript received June 24, 2022; revised August 15, 2022; accepted August 25, 2022. date of publication September 25, 2022; date of current version September 18, 2022.

This work has been supported by the National Natural Science Foundation of China (51907129); Project Supported by Department of Science and Technology of Liaoning Province (2021-MS-236). *(Corresponding Author: Daquan Hao)*

Shengnan Wu is with the School of Electrical Engineering, Shenyang University of Technology, Shenyang 110870, China (e-mail: imwushengnan@163.com).

Daquan Hao is with the School of Electrical Engineering, Shenyang University of Technology, Shenyang 110870, China(e-mail:dq201920269@163.com).

Wenming Tong is with the National Engineering Research Center for Rare Earth Permanent Magnet Machines, Shenyang University of Technology, Shenyang 110870, China (e-mail: twm822@126.com).

Digital Object Identifier 10.30941/CESTEMS.2022.00034

I. Introduction

With the rapid development of China's economy and people's yearning for a better life, motors are more and more widely used in industry and daily life. Hybrid excitation motor has the advantages of electromagnetic uniform adjustment, wide adjustable speed range and high power density. It has a wide application prospect in new energy electric vehicles, wind power generation and other fields [1]. The armature winding and excitation winding of the hybrid excitation synchronous motor studied in this paper are set in the stator slot, which has the characteristics of compact structure, modular splicing of stator teeth and yokes with dovetail slots, and difficult heat dissipation of stator and rotor. It is very important to design a cooling system with high heat dissipation efficiency to reduce the temperature rise of the motor and improve the reliability of the motor.

The existing motor cooling systems are mainly divided into air cooling, liquid cooling and mixed cooling systems. The specific heat capacity of liquid cooling media such as water and oil is larger than that of gas, so the cooling effect is better than air cooling, and it is more suitable for high power density motors [2]-[9]. The most common structure of the motor liquid cooling system is the water jacket embedded in the casing. According to the different structure of the water jacket, it can be divided into circumferential type, spiral type, axial type, etc. Reference [10] analyzes the circumferential, spiral and axial water channels, and analyzes the heat dissipation performance of each water channel. Document [11] Wei Qiang and others also analyzed the triangular rigid channel. Through comparative analysis, the cooling effect is the best. In reference [12], a single water channel is divided into two by using two mutually counter axial water channels, and the water flow directions of the two water channels are opposite, so that the temperature distribution of the motor is relatively uniform. Reference [13] added fins into the cooling channel, fully considered the cooling effect and the pressure drop at the inlet and outlet of the channel, and obtained the optimal parameter design of the spoiler. In reference [14], taking the axial Z-shaped water-cooled motor as an example, the influence of the number of water channels and the structural parameters of water channels on the internal temperature and fluid flow resistance of the motor is studied by using the fluid structure coupling method. The research shows that there is an optimal region for the structural parameters of water channels. Reference [15] has analyzed the heat dissipation effects of three cooling systems, namely, the mixed ventilation spiral channel,

the axial ventilation spiral channel and the axial ventilation straight channel channel. Reference [16] analyzed a hybrid cooling system combining heat pipe and traditional liquid cooling. The distance between the heat source and the coolant of the casing jacket cooling system is far, especially for the rotor, the heat dissipation effect is poor, which affects the safety performance of the motor.

In reference [17], a heat conduction insert is proposed for high-power density permanent magnet motor to cool the end concentrated winding. The heat conduction insert wraps the end winding and extends into the slot to cool the stator winding through heat conduction. However, the heat conduction insert in the groove occupies the space in the groove, which reduces the effective area of the groove. In reference [18], a hybrid cooling technology is proposed for axial flux permanent magnet synchronous motor, including casing cooling water circuit, copper rod inserted into stator teeth, copper rod partially inserted into casing water circuit and directly contacted with coolant, and end winding is filled with glue. Although this cooling method shortens the distance from the heat source, the cooling structure affects the magnetic flux path of the motor, which may lead to saturation of the magnetic density of the stator teeth.

According to the structural characteristics of hybrid excitation synchronous motor with modular stator, the cooling structure of water-cooled plate is designed. The effects of the thickness of water-cooled plate and the number of water channels in the water-cooled plate on the heat dissipation capacity are analyzed by theoretical and computational fluid dynamics (CFD). Based on CFD method, the effects of different water cooling plate structures on flow velocity, pressure drop, pump power consumption and heat dissipation capacity are analyzed. The influence of different water velocity of water inlet pipe on the maximum temperature rise of each part of the motor is analyzed, and the temperature distribution of each part of the motor under the optimal water flow is analyzed. The influence of the traditional spiral water cooling structure and the water cooling plate structure on the heat dissipation capacity of the motor is compared and analyzed. Based on the water-cooled plate cooling structure, the air-water composite cooling structure is designed, and the influence of water-cooled plate cooling structure and air-water composite cooling structure on the maximum temperature rise of each component of the motor is compared and analyzed. It provides a reference for the design of high power density motor cooling system.

II. Motor Model

A. Physical Model

The hybrid excitation synchronous motor studied in this paper has the advantages of high reliability, convenient flux regulation, simple structure and high power / torque density. It has a wide application prospect in the field of new energy electric vehicles. The stator teeth and yokes of the hybrid excitation synchronous motor are of modular structure, which are clamped and fixed through the modular stator teeth and yokes, as shown in Fig. 1 (a) below. The internal part of the motor is a three-dimensional magnetic flux path. The stator teeth are laminated along the axial direction by amorphous alloy strip, and then cut and formed by wire cutting technology; The stator yoke is wound along the radial direction by amorphous alloy material, and then cut and formed by wire cutting technology. Winding the topology of the yoke and laminated teeth can provide three-dimensional magnetic flux path for the motor without the stator magnetic conducting back yoke, thus helping to improve the motor power/torque density. The excitation winding and armature winding are set in the stator slot, as shown in Fig. 1 (b), thus eliminating the brush and collector ring of the excitation winding and enhancing the reliability of the motor.

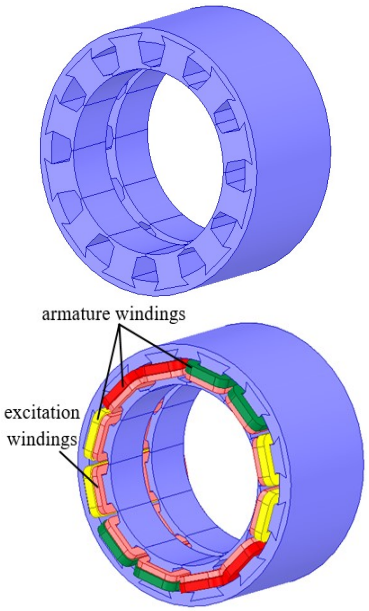

(a) (b)

Fig. 1. Stator structure diagram of modular stator HESM. (a) Modular stator teeth and yoke. (b) Modular stator teeth, stator yoke, armature windings, excitation windings.

The rotor adopts the surface mounted N, S pole permanent magnetic pole and ferromagnetic pole staggered arrangement structure to facilitate the magnetic flux adjustment, as shown in Fig. 2 below. The permanent magnetic pole is made of NdFeB permanent magnetic material. In order to reduce eddy current loss on the ferromagnetic pole, the ferromagnetic pole is made of silicon steel sheet DW310-35 laminated along the axial direction.

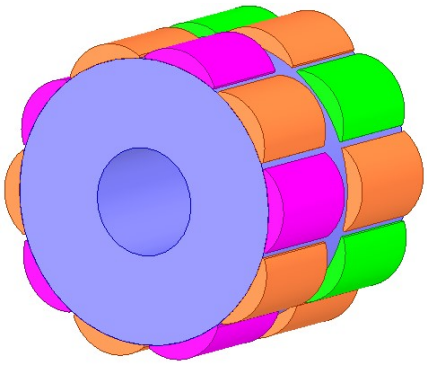

Fig. 2. Rotor structure diagram of modular stator HESM.

The basic parameters of hybrid excitation synchronous motor studied in this paper are shown in TABLE I below.

TABLE I
BASIC PARAMETERS OF HESM

Parameter	Value	Parameter	Value
Rated power P/kW	100	Stator outer diameter D_2/mm	436
Rated speed n/rpm	3000	Stator inner diameter D_{i1}/mm	301
Permanent magnet thickness h_m/mm	16	Air gap δ /mm	2.0
Pole pairs p	5	Axial length L_{ef}/mm	248
Stator slots Q	12	Pole arc coefficient α	0.93

B. Operation Principle and Loss Analysis

Fig. 3 shows the structure of the magnetic flux path of the HESM with a new structure. It can be seen from the figure that the magnetic flux path is a three-dimensional magnetic flux path, including axial magnetic flux, radial magnetic flux and circumferential magnetic flux. The stator teeth provide radial magnetic flux path, and the stator yoke provides axial and circumferential magnetic flux path. The magnetic flux path of permanent magnet is: N-pole permanent magnet→air gap→ stator teeth→stator yoke→ stator teeth→air gap→ S-pole permanent magnet. The electric excitation flux path is: ferromagnetic pole→air gap→stator teeth→ stator yoke→stator teeth→ air gap→ferromagnetic pole. When the electric excitation winding plays the role of magnetization, the permanent magnetic field and the electric excitation magnetic field have the same direction, and the magnetic flux of each pole increases; When the electric excitation winding plays the role of demagnetization, the direction of the permanent magnetic field and the electric excitation magnetic field is opposite, the magnetic flux of each pole is reduced, and the motor operates with weak magnetic field and speed expansion.

Fig. 4 shows the three-dimensional air gap magnetic density distribution of the motor under the independent action of permanent magnet, magnetization increasing operation and demagnetization operation. It can be seen from the figure that the three-dimensional air gap magnetic density and the corresponding permanent magnetic pole and ferromagnetic pole are staggered. When the permanent magnet acts alone, the amplitude of air gap magnetic density under the permanent magnet is 1.1T, there is no magnetic flux on the ferromagnetic pole, and the amplitude of air gap magnetic density under the ferromagnetic pole is close to 0t; Under the magnetization operation state, the air gap magnetic density amplitude at the permanent magnet and under the ferromagnetic pole is 1.1T. At this time, the magnetic flux at each pole increases, and the motor operates at low speed and high torque; Under the demagnetization operation state, the air gap magnetic density amplitude at the permanent magnet is 1.1T, and the air gap magnetic density amplitude under the ferromagnetic pole is 0.6T. The magnetic flux per pole decreases, and the motor operates under the weak magnetic expansion state.

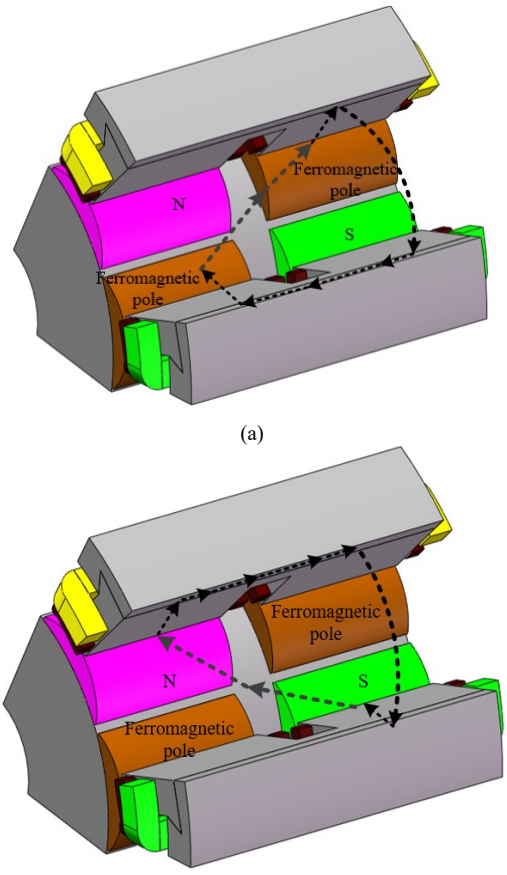

Fig. 3. Structure diagram of HESM flux path. (a) Permanent magnet flux path. (b) Electrically excited flux path.

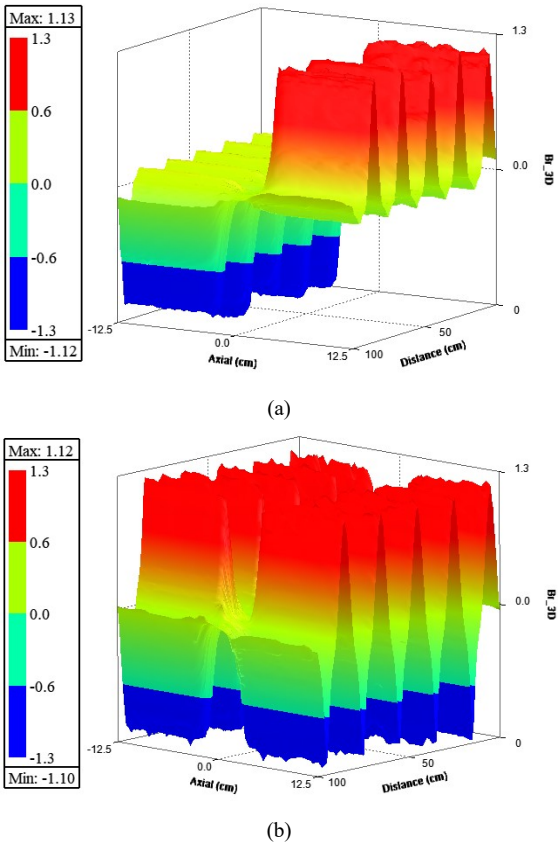

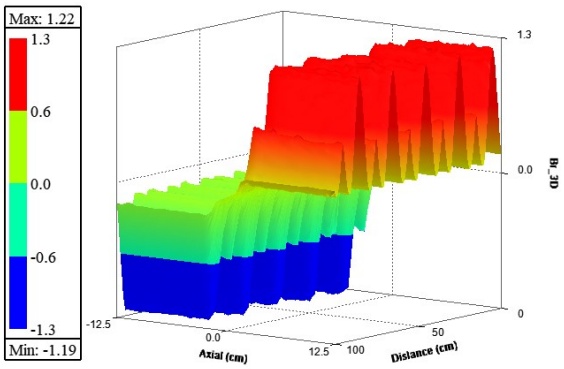

(c)

Fig. 4. Air gap magnetic density under three operating conditions. (a) Rated operation. (b) Magnetization operation. (c) Demagnetization operation

The losses of each part of the motor under rated operation, magnetization and demagnetization are shown in TABLE II. It can be seen that the loss of each component of the motor is high under the demagnetization state, because the motor operates at high speed under the demagnetization state, the frequency is high, and the air gap magnetic field harmonic is large, so the loss is large.

TABLE II
LOSS OF EACH PART OF THE HESM UNDER THREE OPERATING CONDITIONS

Part	Rated operation/W	Magnetization operation/W	Demagnetization operation/W
Stator tooth	1829.2	1849.5	2847.3
Stator yoke	1343.3	1507.1	1722.8
Permanent magnet	616.3	673.0	870.5
Ferromagnetic pole	70.4	80.8	141.0
Armature windings	1081.7	1081.7	1081.7
Excitation windings	0	657.2	657.2

III. ANALYSIS OF COOLING STRUCTURE OF WATER COOLING PLATE

A. Water Cooling Plate Cooling Structure

The structure of the designed water-cooled plate cooling system is shown in Fig. 5. The water cooling plate is Π The number of water-cooling plates is the same as the number of stator teeth of the motor. The stator yoke and the casing are respectively provided with clamping slots. The water-cooling plates are fixed and installed through the clamping slots on the stator yoke and the casing. The water-cooling plates are connected in series with cooling water pipes. The water-cooled plate is set close to the stator teeth and stator yoke, and the armature winding and excitation winding are directly bound to the water-cooled plate. The stator teeth, yoke, armature winding and excitation winding ends are in direct contact with the cooling water plate, which is more conducive to reducing the temperature rise of the motor.

B. Analysis of Cooling Structure of Water Cooling Plate

According to Newton's law of heat dissipation, the heat transferred through thermal convection is:

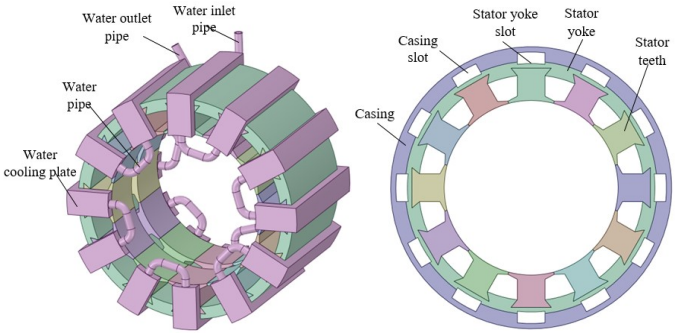

(a) (b)

Fig. 5. Structure diagram of water cooling plate cooling. (a) Water cooling plate and stator teeth and stator yoke. (b) Stator yoke slots and casing slots

$$Q = hA(T_s - T_f) \tag{1}$$

Where, Q is the heat for convective heat transfer; h is the convective heat dissipation coefficient; A is contact area of solid and fluid; T_s is the temperature of solid; T_f is the temperature of fluid.

The hydraulic diameter of the water channel in the water cooling plate is:

$$d = \frac{4S}{C} \tag{2}$$

Where, S is the sectional area of a single flow channel in the water cooling plate; C is the wet circumference of a single channel in the water cooling plate.

The Reynolds number of water in the water cooling plate is:

$$R_e = \frac{vd}{\mu} \tag{3}$$

Where, R_e is the Reynolds number of water; v is the velocity of water; μ is the kinematic viscosity of water.

The Nusselt number of water in the water cooling plate is:

$$N_u = 0.023 R_e^{0.8} P_r^{0.4} \tag{4}$$

Where, N_u is the Nusselt number of water; P_r is the Prandtl number of water.

The convective heat dissipation coefficient of water in the water cooling plate is:

$$h = \frac{N_u A_s}{d} \tag{5}$$

Where, A_s is the thermal conductivity of water.

Bring formulas (2), (3) and (4) into equation (5):

$$h = 0.023(\frac{v}{\mu})^{0.8} P_r^{0.4} A_s \left(\frac{C}{4S}\right)^{0.2} \tag{6}$$

Where, the water flow velocity in the water-cooled plate, the cross-sectional area of the channel in the water-cooled plate, and the wet perimeter affect the convective heat dissipation coefficient of water.

The cooling water flow can be determined by the following formula:

$$P_{loss} = \rho Q_w c_p (T_{out} - T_{in}) \tag{7}$$

Where, P_{loss} is the total loss; ρ is the density of water; Q_w is the volume flow of water; c_p is the specific heat capacity of water; T_{in}、T_{out} is the temperature difference between inlet and

outlet of water.

Relationship between cooling water pump power and differential pressure is:

$$W_{\text{pump}} = Q_{\text{w}} \Delta P \tag{8}$$

$$Q_{\text{w}} = S \times v \tag{9}$$

Where, W_{pump} is the pump power; ΔP is the inlet and outlet pressure difference of water in the water cooling plate.

The structure of a single water-cooling plate is shown in Fig. 6. The wall thickness of the water-cooling plate is 3mm and the width is 48mm of the stator tooth width. Under the same flow rate, the influence of different water-cooled plate thickness and the number of water channels in the water-cooled plate on the convective body field is analyzed, and four water-cooled plate model structures are selected, as shown in the following TABLE III. The number of water channels in structure I, structure II and structure III is 1, the thickness of water cooling plate is 15mm, 17.5mm and 20mm respectively, and the inner diameters of water pipes are 9mm, 11.5mm and 9mm respectively; The number of water channels in structure IV is 3, and the thickness of water-cooling plate is 15mm.

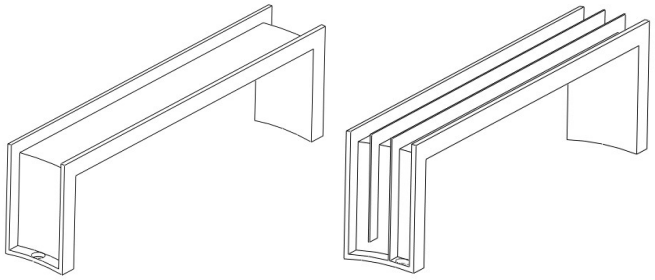

(a) (b)

Fig. 6. Single water cooling plate structure. (a) The number of water channel is 1. (b) The number of water channel is 3.

TABLE III
THERMAL CONDUCTIVITY OF EACH MATERIAL OF MOTOR

cooling structure	structure I	structure II	structure III	structure IV
Plate thickness /mm	15	17.5	20	15
Number of water channels in cooling plate	1	1	1	3
Inner diameter of water pipe /mm	9	11.5	14	9

The comparison between CFD calculation results and theoretical calculation results of the average flow velocity in the water cooling plate and the average convection heat dissipation coefficient of water in the water cooling plate of different model structures is shown in Fig. 7. It can be seen from the figure that the CFD calculation results and the theoretical calculation results have the same trend. Under the same cooling flow, with the increase of the thickness of the water-cooled plate, the average flow velocity and the average convection heat dissipation coefficient in the water-cooled plate gradually decrease; When the thickness of water-cooled plate is the same and the water flow is the same, the increase of the number of water-cooled plates can enhance the heat transfer capacity of water-cooled plates.

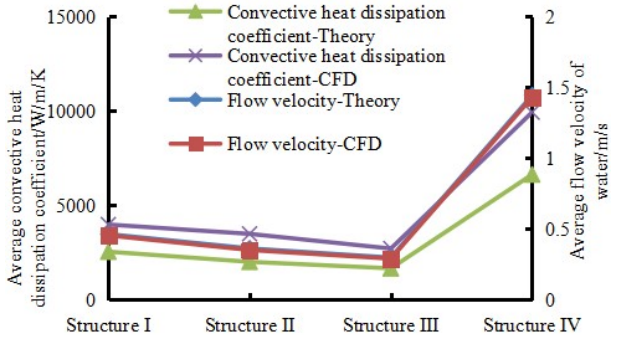

Fig. 7. Comparison between theoretical and CFD calculation results

C. *Fluid field analysis*

The velocity distribution of water in the water cooling plates of different structures is shown in Fig. 8. It can be seen from the figure that the velocity distribution in the water cooling plates of the four structures is relatively uniform, and the velocity in the radial section of the water cooling plate is slightly higher than that in the axial section of the water cooling plate; Under the same flow rate, the flow rate in structure 4 is the highest, with an average flow rate of 1.4m/s. In structures 1-3, with the increase of the thickness of the water-cooled plate, the flow rate in the water-cooled plate gradually decreases.

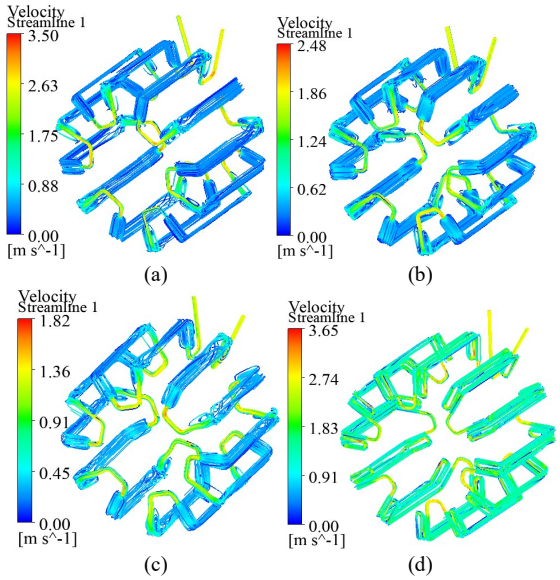

Fig. 8. Velocity distribution of water in water cooling plate. (a) structure I. (b) structure II. (c) structure III. (d) structure IV.

The distribution of convective heat dissipation coefficient of water in the water cooling plate of different structures is shown in Fig. 9. It can be seen from the figure that under the four structures, the distribution of convective heat dissipation coefficient of water in the water cooling plate is relatively uniform, and the convective heat dissipation coefficient of the radial section of the water cooling plate is slightly higher than that of the axial section of the water cooling plate; Under the same flow rate, the convective heat dissipation coefficient of structure IV is the highest, with an average convective heat dissipation coefficient of 9926.9W/m^2/K, and the average convective heat dissipation coefficient of structure I is 3986.2W/m^2/K. When the flow rate and the thickness of the

water-cooled plate are unchanged, the average convective heat dissipation coefficient of structure IV is 2.49 times higher than that of structure I, while the contact area between structure IV and the heat source is 4.8% lower than that of structure I, and the heat dissipation capacity of structure IV is 1.2 times higher than that of structure I; In structures I-III, with the increase of the thickness of the water-cooling plate, the average convective heat dissipation coefficient of the water in the water-cooling plate gradually decreases. The average convective heat dissipation coefficients of the water in structure I-III are 3986.2W/m^2/K, 3491.9W/m^2/K and 2714.5W/m^2/K respectively. The average convective heat dissipation coefficients of the water in structures II and III are 12.4% and 31.9% lower than those in structures I.

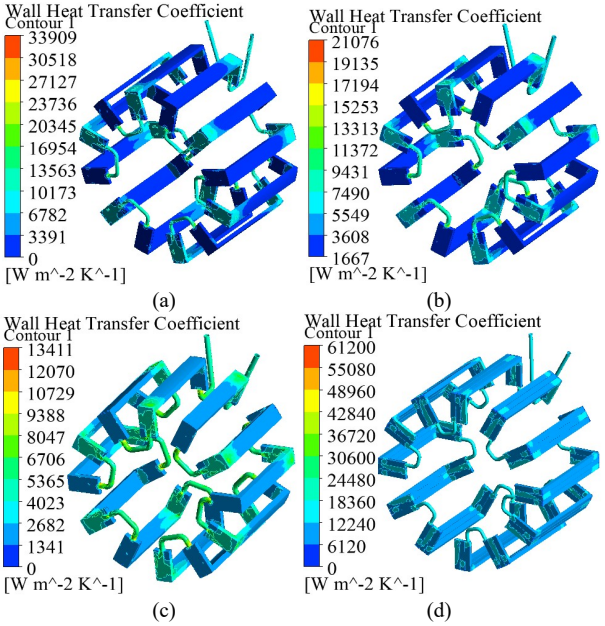

Fig. 9. Distribution of convective heat dissipation coefficient of water in water cooling plate. (a) structure I. (b) structure II. (c) structure III. (d) structure IV.

The pressure distribution of water in the water cooling plate of different model structures is shown in Fig. 10. From the figure, it can be seen that the inlet and outlet pressure differences of water in the water cooling plate of structure I-IV are 101.1kPa, 44.7kPa, 23.7kPa and 302.7kPa, and the power of the water pump of structure I-IV water cooling plate is 17.8W, 7.8W, 4.1W and 53.1W respectively; In structures I-III, with the increase of the thickness of the water cooling plate, the inlet and outlet pressure differences of water in structure II and structure III are reduced by 55.8% and 76.6% respectively compared with those in structure I, and the pump power is reduced by 10.0W and 13.7W respectively; In structure I and structure IV, under the same flow, water cooling plate thickness and pipe diameter, the inlet and outlet pressure difference of water in structure IV is 3 times higher than that in structure I, and the pump power is 35.3W higher.

IV. Analysis of Motor Temperature Field Under Water Cooling System

The fluid structure coupling method is used to analyze and calculate the temperature field of the motor. Firstly, the fluid

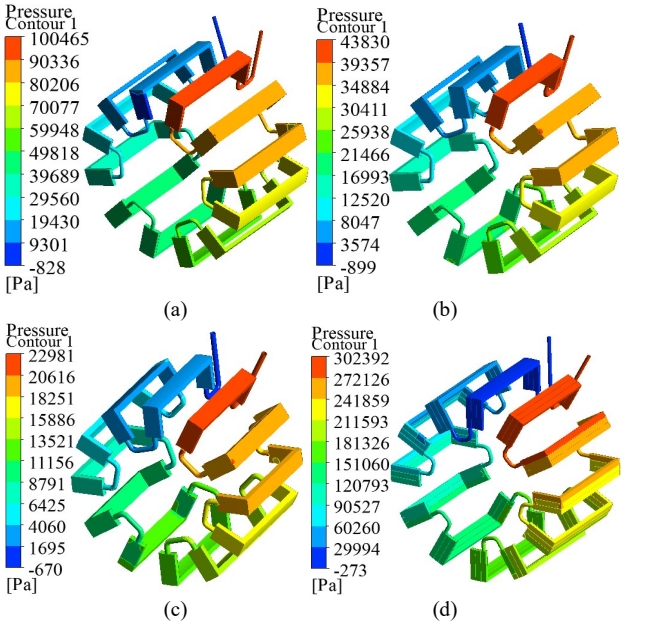

Fig. 10. Pressure distribution of water in water cooling plate. (a) structure I. (b) structure II. (c) structure III. (d) structure IV.

structure coupling analysis model of the motor is established based on reasonable assumptions. There are copper winding, winding paint film, slot insulation, air and impregnation paint in the stator slot of the motor. The filling materials are complex, which is difficult to accurately model one by one, and also affects the mesh generation quality of the model. Therefore, all copper winding and other materials in the slot are equivalent to an isolated entity, and are replaced by an equivalent thermal conductivity.

The material thermal conductivity of each motor component is shown in TABLE IV.The stator teeth and yokes are made of crystalline alloy strips by laminating and winding. In reference [19], the thermal conductivity of amorphous alloy laminationsis measured by the infinite plate layer method. According to the data in reference [19], the thermal conductivity of the stator core in the lamination and winding direction is 0.9W/m/K, The thermal conductivity in other directions is 18W/m/K. The insulation grade of the motor is class F, and the equivalent thermal conductivity of the equivalent insulation is taken as 0.26W/m/K. The rotor core is made of solid low-carbon alloy steel, the casing is made of aluminum alloy, and the rotating shaft is made of No. 10 steel. Its thermal conductivity has mature thermal conductivity data in engineering.

TABLE IV
Thermal Conductivity of Each Component Material

Part	Thermal conductivity / (W/m/K)		
	X direction	Y direction	Z direction
Stator yoke	18	0.9	18
Stator teeth	18	18	0.9
Rotor core	25	25	25
Copper	385	385	385

Equivalent insulation	0.26	0.26	0.26
Permanent magnet	9	9	9
Ferromagnetic pole	39	39	4.43
Casing	168	168	168
Shaft	45	45	45

The volume heat source of each motor component under different operating conditions is shown in TABLE V. It can be seen that the heat source of each part of the motor is high under the maximum demagnetization state, because the motor operates at high speed under the demagnetization state, the frequency is high, and the air gap magnetic field harmonic is large, so the heat source is large.

TABLE V
VOLUME HEAT SOURCE OF EACH COMPONENT

Operating condition	Rated operation / (W/m^3)	Magnetization / (W/m^3)	Demagnetization / (W/m^3)
Stator teeth	223056	225526	347189
Stator yoke	250553	281083	321201
Permanent magnet	612757	669131	865521
Ferromagnetic pole	69998	80338	140196
Armature windings	498410	498410	498410
Excitation windings	0	557891	557891

The boundary conditions are as follows:

(1) Specify the permanent magnet, ferromagnetic pole, rotor core, air gap between the rotating shaft and the machine, and the air contact surface in the end cavity as the rotating surface, and the rotating speed as the rotating speed of the motor.

(2) The natural convection heat dissipation coefficient on the outer surface of the casing, end cover and rotating shaft is set to the empirical value of $30W/m^2/K$.

(3) The ambient temperature is assumed to be 300K.

Calculate the steady-state temperature field of the motor under the maximum demagnetization state and the water-cooled plate structure I. Fig. 11. shows the temperature rise curve of each component of the motor with the flow rate of the water inlet pipe. It can be seen from the figure that the temperature rise of each part of the motor decreases with the increase of flow rate and tends to be stable gradually. After the water velocity of the water inlet pipe reaches 2m/s, the flow rate is 7.6341L/min, and the ability of the water inlet flow rate to reduce the temperature rise of various parts of the motor is limited. At this time, the maximum temperature rise of the rotor of the motor is located in the permanent magnet, which is 126.1K, and the maximum temperature rise of the stator is located in the stator teeth, which is 123.3K.

Fig. 12. is a cloud chart showing the temperature distribution of various parts of the motor when the flow rate of the water inlet pipe is 2m/s. It can be seen from the figure that the maximum temperature rise of the rotor is slightly higher than

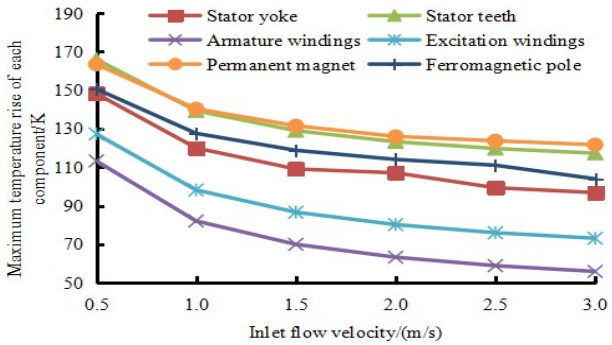

Fig. 11. Curve of maximum temperature rise of motor components with inlet flow velocity.

that of the stator. The maximum temperature rise is located in the middle of the rotor permanent magnet, which is 126.1K. The second is rotor core, which is 120.2K. The maximum temperature rise of ferromagnetic pole is 114.1K. The maximum temperature rise of stator teeth is 123.3K, which is located in the middle of the air contact inside the machine. The highest temperature rise of armature winding is 63.4K in the slot. This is because the end winding is in direct contact with the water-cooled plate for cooling, and the winding in the groove needs insulation with low thermal conductivity to transfer heat to the water-cooled plate, and the thermal resistance is larger than that of the end winding. The maximum temperature rise of the electric excitation winding is 80.3K at the end winding that is not in direct contact with the water-cooled plate. In the circumferential direction, the water temperature of cooling water gradually increases, so the armature winding and electric excitation winding gradually increase along the water flow direction with the increase of water temperature.

Calculate the temperature of each part of the motor under different water flow speed of the traditional shell water cooling, and compare and analyze the temperature rise of each part cooled by the water cooling plate (15mm thick). Fig. 13. shows the spiral water channel of the casing, with the size of 18mm × 28mm, 8 water channels and 5.5mm rib width.

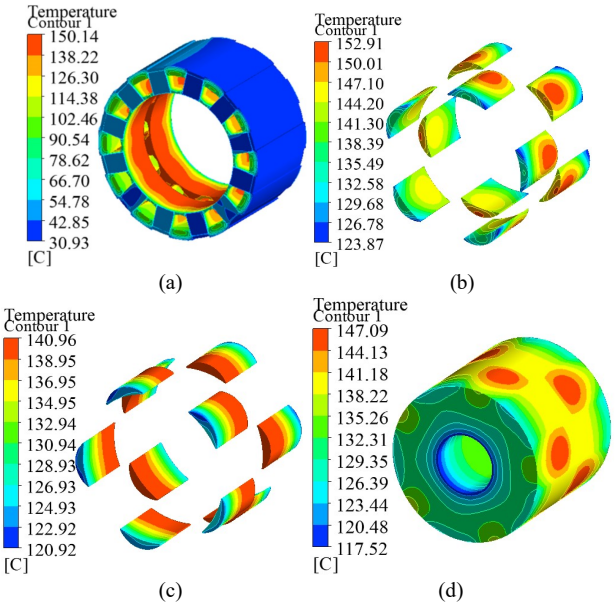

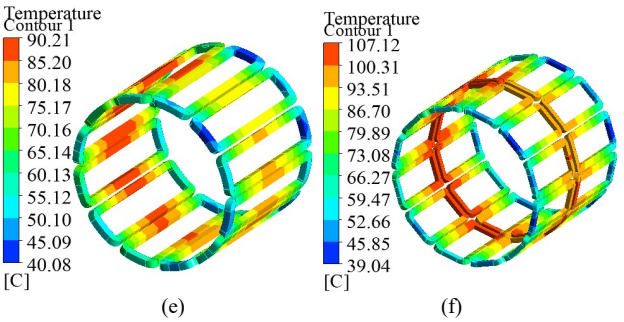

Fig. 12. Cloud diagram of temperature distribution of various parts of motor. (a) Stator yoke and stator teeth. (b) Permanent magnet. (c) Ferromagnetic pole. (d) Rotor core. (e) Armature windings. (f) Excitation windings.

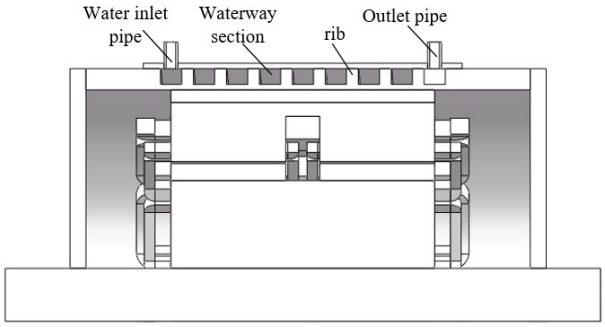

Fig. 13. Structural diagram of spiral water channel of casing.

Fig. 14. shows the maximum temperature rise of each component of the motor under different water inlet pipe flow speeds. From the figure, it can be seen that the maximum temperature rise of each component gradually decreases with the water inlet flow rate and the temperature rise decreases gradually after the water inlet flow rate is 2m/s.

TABLE VI shows the maximum temperature rise of each component under the cooling of the water-cooled plate (15mm thick and 2m/s inlet flow rate) and the spiral channel of the casing (2m/s inlet flow rate). It can be seen from the table that the maximum temperature of each component under the cooling of the spiral water channel of the casing is 2.1-4.1 times higher than that under the cooling of the water-cooled plate. Among them, the maximum temperature rise of the permanent magnet under the cooling of the spiral water channel of the casing is 269.7k, which is 2.1 times higher than that under the cooling of the water-cooled plate. The maximum temperature rises of the armature winding and the electric excitation winding under the cooling of the spiral water channel of the casing are 285.9k and 290.2k respectively, Compared with the maximum temperature rise of armature winding and electric excitation winding under water-cooled plate cooling, it is 4.1 times and 3.6 times higher respectively. Therefore, water-cooled plate cooling can more effectively reduce the temperature rise of the motor and is more suitable for the hybrid excitation motor studied in this paper.

V. Analysis of Fluid Field and Temperature Field of Air-Water Composite Cooling Structure

In order to further reduce the temperature rise of the rotor and the demagnetization risk of the permanent magnet, an air-water composite cooling system is designed on the basis of

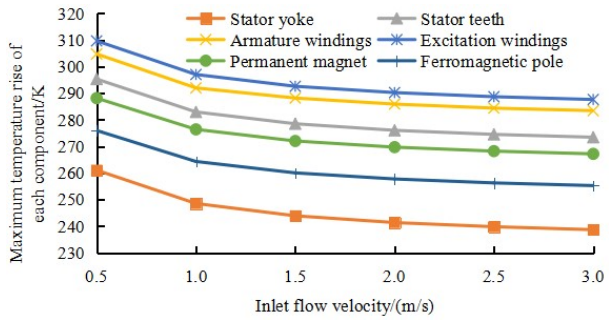

Fig. 14. Curve of maximum temperature rise of each component with inlet water flow rate under cooling of spiral water channel of casing.

TABLE VI
Maximum Temperature Rise of Each Component Under Water Cooling Plate Cooling and Shell Spiral Channel Cooling

Part	Water cooled plate/ K	Casing spiral water channel / K
Stator yoke	107.2	241.3
Stator teeth	123.3	276.0
Permanent magnet	126.1	269.7
Ferromagnetic pole	114.1	257.7
Rotor core	120.2	260.6
Armature windings	63.4	285.9
Excitation windings	80.3	290.2

water-cooled plate cooling, as shown in Fig. 15 below. The solid rotor core is provided with a number of rotor ventilation holes, one end of the rotating shaft is provided with a centrifugal fan, the fan and the rotating shaft rotate synchronously, and an air bag is arranged outside the casing to form an internal circulating air path. When the motor is running, the air in the machine flows from the rotor vent and air gap to the fan end under the drive of the fan. After absorbing the heat of the rotor, it flows to the rotor vent through the enclosure vent and then returns to the rotor vent. The cooling air in the wind pocket transfers the absorbed rotor heat to the outside through the wind pocket, so as to complete the cooling of the rotor. For the cooling structure of air-cooled rotor, the structure is simple, the cost is low, and the temperature rise of the rotor can be effectively reduced.

Fig. 16. shows the distribution cloud diagram of convective heat dissipation coefficient under the rotor ventilation hole composed of circular, semi-circular and rectangular ventilation holes. The area of the rotor ventilation holes under the two

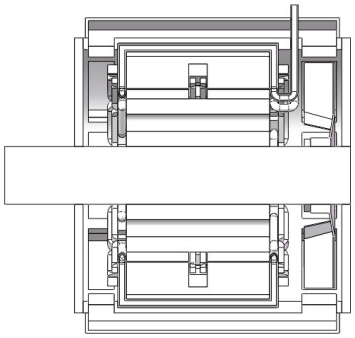

(a)

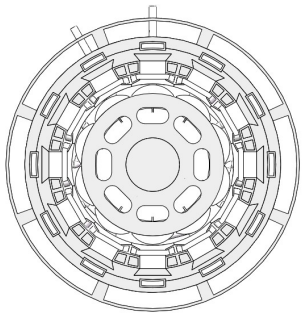

(b)

Fig. 15. Air water composite cooling structure diagram. (a) Side view section. (b) Front view section.

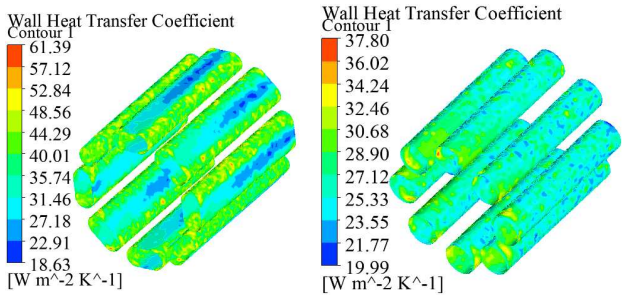

(a) (b)

Fig. 16. Nephogram of convective heat dissipation coefficient distribution of rotor vent. (a) Semi circular and rectangular rotor vent. (b) Circular rotor vent.

structures is the same. It can be seen that the average convective heat dissipation coefficient of the semi-circular and rectangular rotor vent is higher than that of the circular rotor vent.

The structure diagram of cooling fan is shown in Fig. 17. below. The fan is composed of fan blades and end disc. Fan structure parameters include fan outer diameter D_1, fan width b and number of blades N. In order to provide sufficient air pressure, the outer diameter of the cooling fan shall be as large as possible.

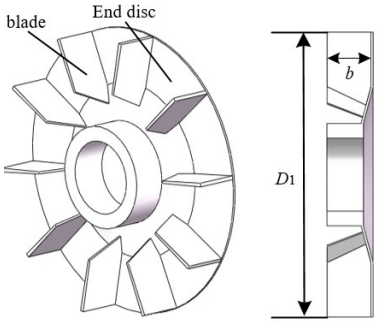

(a) (b)

Fig. 17. Cooling fan structure diagram. (a) three-dimensional view. (b) Side view section.

The fan efficiency is:

$$\eta = \frac{\Delta P Q}{M} \tag{10}$$

Where, ΔP is pressure difference between inlet and outlet of fan, PA; Q is the volume flow of the fan; M is the input power of the fan.

Scheme I: the outer diameter D_1 of the fan is 370mm, the width b of the fan is 30mm, and the number of blades N is 7.

Scheme II: the outer diameter D_1 of the fan is 370mm, the width b of the fan is 45mm, and the number of blades N is 5.

Scheme III: the fan outer diameter D_1 is 390mm, the fan width b is 60mm, and the number of blades N is 5.

The performance calculation results of the three fans are shown in TABLE VII. It can be seen that the cooling mass flow of the three schemes is 0.050kg/s, and the error is within 2%. But the fan efficiency of scheme II is the highest, which is 25.5%, 7.5% higher than that of scheme I; The input power is 4.0% higher than scheme I and 22.6% lower than scheme III. Considering the mass flow, efficiency and input power of the fan, the parameter selection scheme II of the fan.

TABLE VII
PERFORMANCE CALCULATION RESULTS OF THREE FAN PARAMETERS

Scheme	Mass flow Q /(kg/s)	Fan efficiency η /%	Input power M /W
Scheme I	0.050	23.6	96.1
Scheme II	0.051	25.5	100.1
Scheme III	0.050	23.9	122.7

Calculate the steady-state temperature distribution of the motor under the air-water composite cooling system. The water velocity at the inlet of the water pipe is 2m/s, the ambient temperature is 300K, and the inlet water temperature is 300K. The temperature distribution of each part of the motor under the maximum demagnetization state is shown in Fig. 18.

The temperature rise comparison of each part of the motor under the air-water composite cooling system and the water cooling system is shown in TABLE VIII below.It can be seen from TABLE VII below that the maximum temperature rise of all components under the air-water composite cooling system is lower than that of the water-cooled plate cooling structure. The maximum temperature rise of permanent magnet decreased by 18.5K and 14.7%. The maximum temperature rise and fall of stator teeth decreased by 8.0K and 6.5%. The maximum temperature rise of armature winding decreased by 3.0K and 4.7%. The maximum temperature rise of excitation winding is reduced by 6.3K and 7.8%.

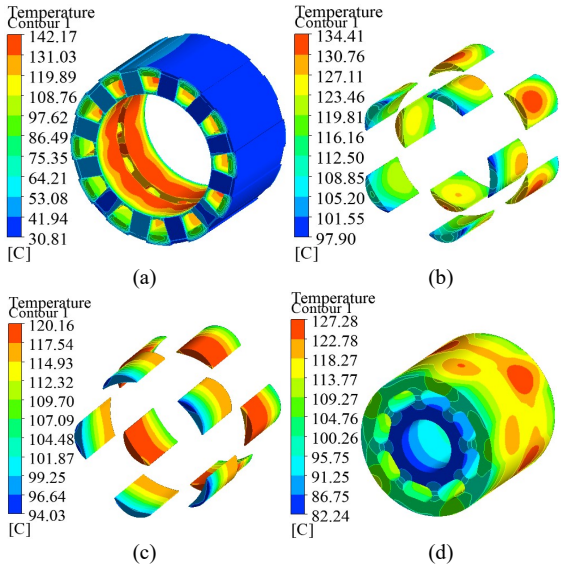

(a) (b)

(c) (d)

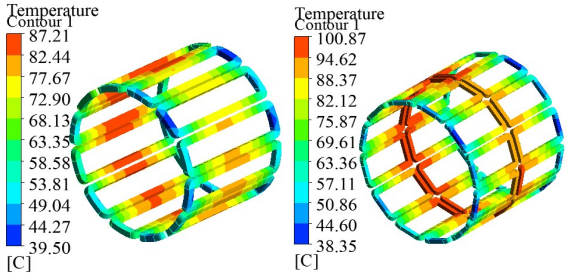

(e) (f)

Fig. 18. Cloud diagram of temperature distribution of various parts of motor. (a) Stator yoke and stator teeth. (b) Permanent magnet. (c) Ferromagnetic pole. (d) Rotor core. (e) Armature windings. (f) Excitation windings

TABLE VIII
MAXIMUM TEMPERATURE RISE OF EACH COMPONENT UNDER WATER COOLING PLATE COOLING AND AIR-WATER COMPOSITE COOLING

Part	Water cooled plate cooling /K	Air water composite cooling /K
Stator yoke	107.2	102.1
Stator teeth	123.3	115.3
Permanent magnet	126.1	107.6
Ferromagnetic pole	114.1	93.3
Rotor core	120.2	100.4
Armature windings	63.4	60.4
Excitation windings	80.3	74.0

VI. CONCLUSION

In this paper, a modular stator hybrid excitation synchronous motor is introduced, and the water-cooled plate cooling structure and air-water composite cooling structure of the motor are designed. The following conclusions can be drawn:

1) Compared with the shell water-cooled structure, the water-cooled plate cooling structure is more conducive to reduce the temperature rise of the motor, and is more suitable for the modular stator motor studied in this paper.

2) Under the condition that the number of water channels and cooling flow in the water-cooled plate remain unchanged, when the thickness of the water-cooled plate is 17.5mm and 20mm, the average convective heat dissipation coefficient of the water in the water-cooled plate is reduced by 12.4% and 31.9% respectively, but the inlet and outlet pressure difference of the water-cooled plate and the pump power are reduced by 55.8% and 76.6% respectively.

3) When the thickness and cooling flow of the water-cooled plate remain unchanged, compared with the case when the number of water channels in the water-cooled plate is 1, when the number of water channels in the water-cooled plate is 3, the heat dissipation capacity of the water-cooled plate is increased by 1.2 times, but the pressure difference at the inlet and outlet of the water-cooled plate and the power of the water pump are increased by 3 times.

4) Compared with the water-cooled plate cooling structure, the maximum temperature rise of permanent magnet, stator core, armature winding and excitation winding under the air-water composite cooling structure is reduced by 14.7%, 6.5%, 4.7% and 7.8% respectively.

REFERENCES

[1] Z. R. Zang, D. Wang and W. Hua, "Overview of configuration, design and control technology of hybrid excitation machines," *Proceedings of the CSEE*, vol. 40, no. 24, pp: 7834-7850, Dec, 2020.

[2] M. Anibal Valenzuela, J. A. Tapia , "Heat transfer design of finned frames for TEFC variable speed motors," *IEEE Trans. Industrial Electronics*, vol. 55, no. 10, pp:3500-3508, Oct , 2008.

[3] S. Ulbrich, J. Kopte , J. Proske, "Cooling fin optimization on a TEFC electrical machine housing using a 2-D conjugate heat transfer model," *IEEE Trans. Industrial Electronics*, vol. 65, no. 2, pp:1711-1718, Feb, 2018.

[4] S. Mizuno, S. Noda, M. Matsushita, et al, "Development of a totally enclosed fan-cooled traction motor," *IEEE Trans. Industry Applications*, vol. 49, no. 4, pp:1508-1514, July-Aug, 2013.

[5] W. M. Tong , S. N. Wu and R. Y. Tang, "Totally enclosed self circulation axial ventilation system design and thermal analysis of a 1.65MW direct drive PMSM," *IEEE Trans. Industry Applications*, vol. 65, no. 12, pp:9388-9398, Dec, 2018.

[6] G. J. Zhu, X. M. Liu, H. Chen, et al, "Cooling system of high speed PMSM based on a coupled fluidic thermal model," *IEEE Trans. Applied Superconductivity*, vol. 29, no. 2, pp:1-5, Mar, 2019.

[7] V. Ruuskanen, J. Nerg, M. Niemela, et al, "Effect of radial cooling ducts on electromagnetic performance of the permanent magnet synchronous generators with double radial forced air cooling for direct driven wind turbines," *IEEE Trans. Magnetics*, vol. 49, no. 6, pp:2947-2981, Jun, 2013.

[8] X. G. Fan, R. H. Qu, J. Li, "Ventilation and thermal improvement of radial forced air cooled FSCW permanent magnet synchronous wind generators," *IEEE Trans. Industry Applications*, vol. 53, no. 4, pp:3447-3456, July-Aug, 2017.

[9] K. Yang, Y. J. Feng, "Design of novel spiral magnetic poles and axial cooling structure of outer rotor PM torque motor," *IEEE Trans. Applied Superconductivity*, vol. 20, no. 3, pp:838-841, Jun, 2010.

[10] X. Y. Hang, H. W. Zhang, X. Xu, et al, "Design of cooling system for amorphous alloy axial flux permanent magnet motor based on computational fluid dynamic," *Transactions of China Electrotechnical Society*, vol. 32, no. 20, pp:189-197, Oct, 2017.

[11] Q. Wei, G. H. Feng and B. Y. Zhang, "Cooling system of direct drive PMSM for mining belt conveyor," *Journal of Mechanical and Electrical Engineering*, vol. 36, no. 8, pp:873-878, Aug, 2019

[12] X. Y. Li, Z. G. Tang, D. Y. Zhang, et al, "Analysis of heat dissipation characteristics of double channel liquid cooled permanent magnet synchronous motor," *Journal of Hefei University of Technology*, vol. 41, no. 6, pp:726-730, Jun, 2018.

[13] J. X. Hao, Z. G. Tang, H. Q. Li, et al, "Optimization design of the spoiler in cooling channe of liquid-cooled motor," *Journal of Hefei University of Technology*, vol. 39, no. 4, pp:440-444, Apr, 2016.

[14] C. P. Li, F. Chai, X. I. Feng, et al, "Optimization design and analysis of cooling system used for mini electric vehicle motor," *International Conference on Electrical Machines and Systems(ICEMS)*, Hangzhou, China, 2014, pp:2413-2417.

[15] F. G. Zhang, G. H. Du, T. Y. Wang, et al, "Temperature field analysis of 1.12MW high speed permanent magnet machine with different cooling schemes," *Transactions of China Electrotechnical Society*, vol. 29, no. S1, pp. 66-72, Sep, 2014.

[16] S. Y. Ding, Z. Q. Sun, D. G. Xu, et al, "Numerical Investigation of Heat Transfer for3 MW Doubly-fed Wind Generator," *Proceedings of the CSEE*, vol. 32, no, 3, pp:137-143, Jan, 2012.

[17] H. Vansompel, P. Sergeant, "Extended end winding cooling insert for high power density electric machines with concentrated winding," *IEEE Trans. Energy Conversion*, vol. 35, no. 2, pp. 948-955, Jun, 2019.

[18] M. Polikarpova, P. Ponomarev, P. Lindh, et al, "Hybrid cooling method of axial flux permanent magnet machines for vehicle applications," *IEEE Trans. Industrial Electronics*, vol. 62, no 12, pp:7382-7390, Dec, 2015.

[19] W. M. Tong, J. Y. Sun, X. B. Cheng, et al, "Thermal conductivity measurement of amorphous alloy laminated core and thermal analysis of amorphous alloy motor," *Transactions of China Electrotechnical Society*, vol. 32, no. 15, pp. 42-49, Aug, 2017.

Shengnan Wu (M'18) was born in Yingkou, China. She received the B.S., M.S., and Ph.D. degrees in electrical engineering from the Shenyang University of Technology, Shenyang, China, in 2008, 2011, and 2017, respectively.

She is currently a Postdoctoral Research Assistant in electrical engineering with Shenyang University of Technology. Her research interests include electromagnetic design and multiphysical field simulation and analysis of permanent magnet machines.

Daquan Hao was born in Liaoning, China. He received the B.S. degree in electrical engineering from Liaoning Shihua University, Fushun, China, in 2019. He is currently working toward the M.S. degree in electrical engineering with the Shenyang University of Technology, Shenyang, China.

His main research interests include multiphysical field simulation and analysis of permanent magnet machines.

Wenming Tong (M'18) was born in Dandong, China. He received the B.S. and Ph.D. degrees in electrical engineering from the Shenyang University of Technology, Shenyang, China, in 2007 and 2012, respectively. He is currently an Associate Professor with the National Engineering Research Center for Rare Earth Permanent Magnet Machines, Shenyang University of Technology.

His major research interests include the design, analysis, and control of high-speed and low-speed direct drive permanent magnet machines, axial flux permanent magnet machines, hybrid excitation machines, and high-performance machines with new types of soft magnetic materials.